Check for updates

Acridones as promising drug candidates against Oropouche virus

Marielena Vogel Saivish [a,1], Gabriela de Lima Menezes [b,c,1], Roosevelt Alves da Silva [b], Leticia Ribeiro de Assis [d], Igor da Silva Teixeira [a], Umberto Laino Fulco [c], Clarita Maria Secco Avilla [a,d], Raphael Josef Eberle [e,f], Igor de Andrade Santos [g], Karolina Korostov [e], Mayara Lucia Webber [a], Gislaine Celestino Dutra da Silva [a], Maurício Lacerda Nogueira [a], Ana Carolina Gomes Jardim [d,g], Luis Octavio Regasin [d], Mônika Aparecida Coronado [e,*], Carolina Colombelli Pacca [a,d,*]

[a] Laboratório de Pesquisas em Virologia, Departamento de Doenças Dermatológicas, Infecciosas e Parasitárias, Faculdade de Medicina de São José do Rio Preto, São José do Rio Preto, SP 15090-000, Brazil
[b] Unidade Especial de Ciências Exatas, Universidade Federal de Jataí, Jataí, GO 75801-615, Brazil
[c] Bioinformatics Multidisciplinary Environment, Programa de Pós-graduação em Bioinformática, Universidade Federal do Rio Grande do Norte, Natal 59078-400, RN, Brazil
[d] Institute of Biosciences, Humanities and Exact Sciences, São Paulo State University, São José do Rio Preto, SP 15054-000, Brazil
[e] Institute of Biological Information Processing (IBI-7: Structural Biochemistry), Forschungszentrum Jülich, Jülich 52428, Germany
[f] Heinrich Heine University Düsseldorf, Faculty of Mathematics and Natural Sciences, Institute of Physical Biology, Universitätsstraße, Düsseldorf 40225, Germany
[g] Institute of Biomedical Sciences, Federal University of Uberlândia, Uberlândia-MG 38405-302, Brazil

A R T I C L E   I N F O

A B S T R A C T

Oropouche virus (OROV) is an emerging vector-borne arbovirus found in South America that causes Oropouche fever, a febrile infection similar to dengue fever. It has a high epidemic potential, causing illness in over 500,000 cases diagnosed since the virus was first discovered in 1955. Currently, the prevention of human viral infection depends on vaccination, but availability for many viruses is limited, and they are classified as neglected viruses. At present, there are no vaccines or antiviral treatments available. An alternative approach to limiting the spread of the virus is to selectively disrupt viral replication mechanisms. Here, we demonstrate the inhibitory effect of acridones, which efficiently inhibited viral replication by 99.9 % *in vitro*. To evaluate possible mechanisms of action, we conducted tests with dsRNA, an intermediate in virus replication, as well as MD simulations, docking, and binding free energy analysis. The results showed a strong interaction between FAC21 and the OROV endonuclease, which possibly limits the interaction of viral RNA with other proteins. Therefore, our results suggest a dual mechanism of antiviral action, possibly caused by ds-RNA intercalation. In summary, our findings demonstrate that a new generation of antiviral drugs could be developed based on the selective optimization of molecules.

1. Introduction

Oropouche virus (OROV) belongs to the *Orthobunyavirus* genus of the *Peribunyaviridae* family, one of the largest and most diversified families of RNA virus that include multiple emerging human pathogens (Mourão et al., 2009, pp. 2007–2008; Travassos da Rosa et al., 2017). Since the 1960s, Oropouche virus (OROV) has caused periodic outbreaks of a debilitating febrile illness, with more than 30 epidemics and 500,000 infected people in Brazil, Peru, Trinidad, Panama, and Suriname. It is a potential candidate for future emerging epidemics in the South and Central America region (Pereira et al., 2021; Silva-Caso et al., 2019; Travassos da Rosa et al., 2017). OROV has caused several outbreaks, and sporadic infections in the Brazilian Amazon and evidence suggests the circulation of virus in other Brazilian states (Azevedo et al., 2007; Cardoso et al., 2015; da Costa et al., 2017), has demonstrated that OROV is spreading to the exterior of endemic locales. As a result, OROV has been

identified as a potential candidate for an epidemic (de Souza Luna et al., 2017; Gutierrez et al., 2020; Romero-Alvarez and Escobar, 2018; Silva-Caso et al., 2019; Travassos da Rosa et al., 2017).

The severity of the disease varies and ranges from a self-limiting febrile illness to encephalitis and hemorrhagic fever. In humans, OROV can cause a severe febrile illness associated with headache, myalgia, arthralgia, malaise, migraine, restlessness, nausea, vomiting, dizziness, and skin rash (Travassos da Rosa et al., 2017). Hemorrhagic phenomena (petechiae, epistaxis, and gingival bleeding) have been reported in some patients (Mourão et al., 2009). While most patients with Oropouche fever recover within 2 to 3 weeks of the initial infection without long-term sequelae, symptoms can persist for months, and surprisingly, relapses are common (Pinheiro et al., 1981). In some patients, OROV infection progresses to meningitis and/or encephalitis (Pinheiro et al., 1982), and this neurotropism is also demonstrated *in vitro* (Almeida et al., 2021; Santos et al., 2014). Indeed, OROV was detected in the cerebrospinal fluid of almost 7 % of patients with meningoencephalitis who were suspected of having an acute viral infection of the central nervous system (CNS) in certain settings (Bastos et al., 2012, 2014). Neurological signs and symptoms in patients with OROV include vertigo, lethargy, diplopia, nystagmus, and nuchal rigidity (Pinheiro et al., 1982).

Despite the rising danger of the virus, no vaccine or specific antiviral therapy is approved against OROV infection, and existing literature describing a potential antiviral candidate against OROV is limited. The treatment of symptomatic Oropouche virus (OROV) infections is palliative, based on the use of non-salicylate analgesics and non-steroidal anti-inflammatory drugs (Sakkas et al., 2018). Considering the potential epidemiological importance of these viruses, the search for compounds with anti-OROV activity may provide a potential alternative.

The molecular class of acridone compounds has attracted attention in recent years for its wide range of biological properties, including selective inhibition of various human pathogenic DNA and RNA viruses (Gensicka-Kowalewska et al., 2017; Gláz et al., 1973; Mazzucco et al., 2015; Tonelli et al., 2011). Their precise mode of action is not clearly determined, although the predominant action seems to be centered on synthesizing nucleic acids (Mazzucco et al., 2015). As part of our continuing investigations on antiviral acridones (Campos et al., 2017), we identified FAC21 and FAC22 (Fig 1), which present antiviral activity against OROV, with a mechanism of action based on intercalation into the dsRNA, an intermediate of virus replication, and inhibitory interactions on the endonuclease virus protein.

2. Materials and methods

2.1. Synthesis of FAC21

The synthesis of FAC 22 was achieved in two steps using Ullmann and intramolecular acylation(Sánchez et al., 2006). Step 1. A mixture of 2-chloro-3,4-dimethoxybenzoic acid (10 mmol), 3,4,5-trimethoxyaniline (15 mmol), anhydrous K_2CO_3 (15 mol L^{-1}) and Cu (200 mg) in 1-pentanol (120 mL) was stirred at reflux temperature for 8 h. The cooled mixture was acidified with HCl (2 mol L^{-1}), and the resulting product was extracted with ethyl acetate (3 × 75 mL). The organic layers

were dried, filtered and concentrated under reduced pressure. The crude product was subjected to column chromatography over silica gel eluting with hexane and ethyl acetate (3:7) to give anthranilic acid derivative (AAD) (48 %). Step 2. A suspension of AAD (3 mmol) and polyphosphoric acid (30 mL) was vigorously stirred at 150 °C for 12 h. The cooled mixture was solubilised in cooled hexane (250 mL). The precipitate was submitted to the chromatography column over silica gel eluting with hexane and ethyl acetate (1:1) to furnish FAC 21 (32 %).

2.2. Synthesis of FAC22

The synthesis was carried out as previously described (Herath et al., 2004). A mixture of 3-amino-2-naphthoic acid (1 g), anhydrous phloroglucinol (1.2 g) and para-toluene sulphonic acid (PTSA, 50 mg) in 1-hexanol (30 mL) was refluxed for 6 h. The mixture was allowed to cool, stirred with 100 mL of hexane and filtered. The residue product was washed with hexane (3 × 100 mL and dichloromethane (2 × 100 mL) to remove 10-hexanol and traces of 3-amino-2-naphthoic acid and PTSA. The dried crude product was submitted to the chromatography column over gel silica gel, eluting with hexane and ethyl acetone (7:3), yielding FAC22 (32 %).

The structures of FAC21 and FAC22 were confirmed by analysis of Nuclear Magnetic Resonance (NMR) spectra, including ^{1}H and ^{13}C NMR experiments. Chemical shifts were expressed in ppm. Coupling constants (*J*) were expressed in Hz, and splitting patterns are described as follows; *s* = singlet, br = broad singlet, *d* = doublet; dd = double of doublets, ddd – double of doublets. Spectra were recorded on a Varian INOVA-500 spectrometer (11.7 T). ^{1}H and ^{13}C NMR spectra were presented in the supplementary material.

1,2,3,5,6-Pentamethoxy-9-(10*H*)-acridinone (FAC 22): amorphous orange-red powder. ^{1}H NMR (500 MHz, DMSO-d_6): 7.27 (s; H-4), 7.02 (d; *J* = 9.0 Hz; H-7), 7.89 (d; *J* = 9.0 Hz; H-8), 10.6 (s; H-10), 3.80 (s; 1-OMe), 3.87 (s; 2-OMe), 3.76 (s; 3-OMe), 3.90 (s; 5-OMe) and 3.93 (s; 6-OMe). ^{13}C NMR (125 MHz, DMSO-d_6): 153.0 (C-1), 134.0 (C-2), 157.2 (C-3), 95.2 (C-4), 134.7 (C-5), 154.1 (C-6), 107.1 (C-7), 122.0 (C-8), 174.5 (C-9), 140.3 (C-4a), 137.0 (C-5a), 116.7 (C-8a), 109.2 (C-9a), 60.5 (1-OMe), 61.5 (2-OMe), 60.9 (3-OMe), 56.1 (5-OMe) and 55.7 (6-OMe).

1,3-Dihydroxybenzo[*b*]acridin-12(5*H*)-one (FAC 23): amorphous orange-red powder. ^{1}H NMR (500 MHz, DMSO-d_6): 5.98, (d; *J* = 2.5 Hz; H-2), 6.29 (d; *J* = 2.5 Hz; H-4), 11.1 (s; H-5), 7.83 (s; H-6), 7.95 (d, *J* = 8.0 Hz; H-7), 7.58 (ddd; *J* = 2.0, 8.0 and 8.0 Hz; H-8), 7.41 (ddd; *J* = 2.0, 8.0 and 8.0; H-9), 8.12 (d; *J* = 8.0 Hz; H-10), 8.85 (s; H-11), 14.1 (s; 1-OH) and 10.7 (s; 3-OH). ^{13}C NMR (125 MHz, DMSO-d_6): 165.1 (C-1), 94.9 (C-2), 164.1 (C-3), 90.9 (C-4), 111.3 (C-6), 126.4 (C-7), 126.5 (C-8), 126.4 (C-9), 127.7 (C-10), 129.5 (C-11), 180.9 (C-12), 144.5 (C-4a), 137.4 (C-6a), 128.6 (C-10a) and 101.9 (C-12a).

2.3. Cell culture and virus

Vero cells were culture grown in Minimal Essential Medium (MEM) (Gibco, Waltham, MA, USA) supplemented with 10 % (v/v) heat-inactivated fetal bovine serum (FBS) (Gibco, Waltham, MA, USA), 100 U mL^{-1} of penicillin, 0.1 mg mL^{-1} of streptomycin, and 0.5 μg mL^{-1} of amphotericin B (Gibco, Waltham, MA, USA) was incubated at 37 °C in
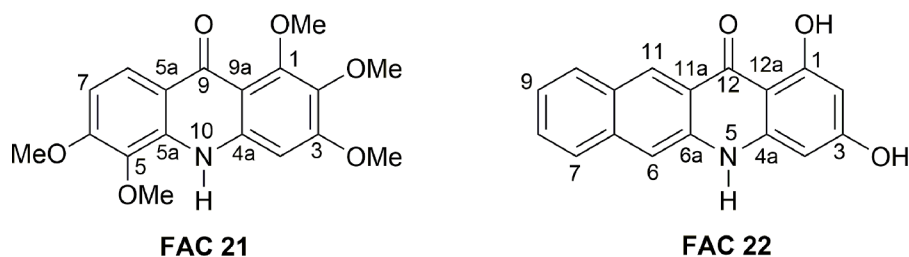

Fig. 1. Chemical structure of the acridones FAC21 and FAC22.

a humidified atmosphere containing 5 % CO_2. The C6/36 cells were culture in Leibovitz-15 medium (L-15) with 10 % FBS at 28 °C. Oropouche virus (strain BeAn 19,991) stocks were propagated in C6/36 cells and titrated in Vero cells using plaque-forming assay (PFU), described below.

2.4. Virus plaque-forming units assay

Briefly, Vero cells grown in a 24-well culture plate were infected by 0.1 mL of ten-fold dilutions of supernatants. Following an incubation of 1 h at 37 °C, 0.5 mL of culture medium supplemented with 2 % FBS and 1.5 % carboxymethylcellulose sodium salt (Sigma-Aldrich, Saint-Quentin-Fallavier, France) were added, and the incubation was extended for three days at 37 °C. After removing the media, the cells were fixed (formaldehyde 10 %) and stained with 2 % crystal violet diluted in 20 % ethanol. Plaques were counted and expressed as plaque-forming units per milliliter ($PFU·mL^{-1}$).

2.5. Viral infection assay

Viral infection experiments were performed in Vero cells seeded in 24-well plates pre-infected with a multiplicity of infection (MOI) of 0.1 for the virus tested. Then, we washed the wells with PBS to remove the viral inoculum and incubated them with DMSO or FACs at the indicated concentrations and times. Cell supernatants were harvested to quantify the viral titers using a plaque-forming assay described above.

2.6. dsRNA intercalation assay

To investigate the compounds' potential to interact with dsRNA as a potential mode of action (Campos et al., 2017; Krawczyk et al., 2009; Silva et al., 2019), the HCV JFH-1 3′ untranslated region (UTR) was amplified employing primers flanked by a T7 promoter site, being the primers and template described by Campos et al., 2017; Krawczyk et al., 2009. The product was purified by ReliaPrep™ DNA Clean-Up and Concentration System (Promega®) and used for *in vitro* transcription by the HiScribe™ T7 High Yield RNA Synthesis Kit (New England Bio-Labs®) (Campos et al., 2017; Krawczyk et al., 2009; Silva et al., 2019). The dsRNA molecule was obtained by complementary annealing and incubated with FAC21 and 22 at 18.5 μM for 45 min and analyzed in 1 % agarose 1X TAE gel stained with ethidium bromide. The lack of band in the gel suggests the compound-dsRNA interaction by impairing the intercalation with ethidium bromide. Doxorubicin (100 μM) was used as a positive control of the interaction. The band quantification was performed using ImageJ.JS version 1.53j.

2.7. Cloning

The codon-optimized cDNA encoding endonuclease protein (residues 1–179; GenBank Protein Accession number AJE24678.1) of OROV RNA-polymerase was synthesized implemented in the Kanamycin resistant vector pET-24a(+). The construct contains an N-terminal hexahistidine affinity tag and a TEV protease cleavage site.

2.8. Protein expression and purification

Endonuclease domain-pET-24a(+) vectors were transformed into *E. coli* Rosetta (DE3) (Novagen) competent cells and grown overnight at 37 °C in SOC medium. The pre-culture was added to fresh LB-medium plus kanamycin and chloramphenicol and grew at 37 °C until the cells reached OD_{600} between 0.6 – 0.8. The culture was induced with 0.5 mM IPTG and incubated for 5 h at 37 °C and 120 rpm. After the cells were harvested, the pellet was dissolved in 3 M Guanidine; 20 mM Tris_HCl, 500 mM NaCl, 1 mM ß-mercaptoethanol, pH 8.0 at room temperature for 30 min and subsequently centrifuged at 7000 rpm, 10 °C for 60 min, followed by filtration (0.45 μm) and loaded onto Ni-NTA column pre-

equilibrated with the same buffer. The protein was eluted with 500 mM imidazolium. The eluted fraction was dialysed against 3 M GdmCl, 10 mM Tris–HCl, 100 mM Sodium phosphate, 10 mM ß-mercaptoethanol, and pH 8.0 to remove the Imidazolium. The protein refolding was performed using 10 mM Tris–HCl, 100 mM Sodium phosphate, pH 8.

2.9. Activity assay

OROV endonuclease activity assay was performed as described previously for viral endonuclease (Noble et al., 2012), using the DNA substrate FAM-TCT CTA GCA GTG GCG CC-TAM (Integrated DNA Technologies, Coralville, USA) at a concentration of 2 μM. The reaction buffer contained 50 mM Hepes pH 7.5, 150 mM KCL and 1 mM $MnCL^2$. Reactions utilized 320 nM OROV endonuclease in 60 μL volume reactions using an Infinite 200 PRO plate reader (Tecan, Männedorf, Switzerland). The assay was performed in Corning 96-well plates (Merck, Darmstadt, Germany), and the fluorescence intensities were measured at 60 s intervals over 60 min at 37 °C. The excitation and emission wavelengths were 495 nm and 520 nm, respectively.

Inhibition of OROV endonuclease activity by molecules FAC21 and FAC22 was investigated using the activity assay described above. 50 μM of the compounds were used for an initial screening test, and 50 μM EDTA was used as a known inhibitor control.

For half-maximal concentration (IC_{50}) determination, the protein was incubated with 0–90 μM FAC21 for 10 min at room temperature. All inhibition assays were performed as triplicates, and the results are shown as mean ± standard deviation (SD). Each experiment was performed with freshly purified protein. The IC_{50} value was calculated by plotting the initial velocity against various concentrations of the combined molecules using a dose-response curve in GraphPad Prism5 software (San Diego, CA, USA), and data are presented as mean ± SD. The inhibition mode of FAC21 was determined using different final concentrations of the inhibitor and substrate. 320 nM OROV endonuclease was incubated with the inhibitor in various concentrations for 10 min at RT. Subsequently, the reaction was initiated by the addition of the corresponding concentration series of the substrate. The data were analyzed using a Lineweaver-Burk plot; therefore, the reciprocal of velocity (1/V) *vs* the reciprocal of the substrate concentration (1/[S]) was compared (Motulsky and Christopoulos, n.d.). All measurements were performed in triplicate, and data are presented as mean ± SD.

2.10. Statistical analysis

All data are expressed as the mean ± standard deviations (SDs). The statistical significance of the mean values' differences was assessed with one-way analyses of variance (ANOVA), followed by Tukeys' multiple comparison test. Significant differences were considered at $p < 0.01$ (**) and $p < 0.0001$ (****). A standard two-way ANOVA and subsequent Dunnett's test was used to analyze the antiviral effect of FAC21 and FAC22. All statistical analyses were performed with GraphPad Prism8 software (San Diego, CA, USA).

2.11. Modeling of N-terminal OROV endonuclease domain protein

The crystallographic structure of the N-terminal polymerase of OROV is not yet available in the Protein Data Bank (PDB). Therefore, the N-terminal sequence (1–180) comprising the endonuclease domain of the protein was retrieved from the GenBank database (accession code: AJE24678) for molecular modeling in the I-TASSER server. The coordinates of the initial model were submitted to the MolProbity server (Williams et al., 2018) to assess the quality of the model. The manganese ion (Mn^{2+}) was inserted into the model by overlaying it with the N-terminal endonuclease structure of the *La Crosse* virus (PDB ID: 2XI5) because the output model does not contain the Mn^{2+}. After this step, the PropKa server (Olsson et al., 2011) was used to predict the protonation state of the amino acid side chains at physiological (7.4) pH.

2.12. Molecular dynamic (MD) simulations without ligand

Before ligand docking, a molecular dynamics (MD) simulation of the N-terminal endonuclease domain of OROV was performed. Three identical systems were prepared and subjected to MD with a time duration of 200 nanoseconds (ns). Simulations were performed using GROMACS 2020.3 Software (Abraham et al., 2015) with the Amber ff99SB-ILDN force field. The Mn^{2+} parameter is not available in this force field/GROMACS version. To enable the simulation of metal ion proteins, the Mn^{2+} parameters for Amber force fields were retrieved from http://amber.manchester.ac.uk and inserted into the corresponding force field files.

The protein was embedded in a cubic simulation box with edges spanning at least 12 Å away from the solute surface filled with a three-site (TIP3P) water model. Each system was then neutralized with four sodium (Na^+) ions to undergo a minimisation step.

The minimisation step is necessary to ensure that the system does not have steric conflicts or improper geometry after water addition. The procedure was performed in a two-step energy minimisation. The first step consisted of a maximum of 500 steps or when the maximum force in any atom reached a value below 50 kJ/mol/nm, using the steepest descent algorithm with protein restraint, focusing on solvent relaxation. The second minimisation step was performed without protein restraint in flexible water, using the same steepest descent algorithm. In addition, the number of maximum steps was increased to 10,000 steps or when the force applied in the atom reached a value less than 250 kJ/mol/nm.

After ensuring a suitable geometry and solvent orientation for the initial structure, the next step is equilibrating the solvent and ions around the protein. The pressure and temperature of the system were set to 1 atm and 310 K in two separate 100 picoseconds (ps) steps, referred to as the NVT ensemble (temperature setting) and NPT ensemble (pressure setting). For this purpose, the modified Berendsen (Berendsen et al., 1984) and Parrinello-Rahman (Hutter, 2012) algorithms were applied to adjust the system temperature and pressure, respectively. In both steps, bonds with hydrogen were constrained by the LINCS algorithm (Hess et al., 1997), and positional restraints were applied in the protein to equilibrate the solvent around the solute.

The Particle Mesh Ewald summation method was used to calculate long-range electrostatic interactions, and a cut-off of 1 nm was defined for non-bonded interactions. Finally, the leap-frog algorithm (Hockney et al., 1974) was used to integrate the equations of motion, with a time step of 0.2 femtoseconds (fs). Before the MD run, a small NPT ensemble of 1 ns was performed with no restriction on protein position, and the production run of each identical system was performed at 200 ns with no restriction on protein conformation. A total of 2000 protein frames were produced from each MD run. Each run is referred to here as a replicate.

The MD trajectories were visualized using UCSF Chimera software (Pettersen et al., 2004). The root means square deviation (RMSD) and fluctuation (RMSF) were calculated using the "gmx" commands of the GROMACS package. All plots were generated using the R language in RStudio (RStudio Team, 2021) version 4.1.1, and protein image representations were generated in UCSF ChimeraX (Pettersen et al., 2021).

2.13. Ensemble docking

AutoDock Vina 1.2.2 software (referred to here only as Vina) was used for docking (Trott and Olson, 2010). First, the 3D structure of the FAC21 was retrieved from the PubChem database (https://pubchem.ncbi.nlm.nih.gov/compound/Wedelolactone) in SDF format. The molecule was converted to PDB format using Marvin Sketch software (https://www.chemaxon.com/). The appropriate ligand format for Vina docking is PDBQT. OpenBabel software (O'Boyle et al., 2011) was used to convert PDB to PDBQT, setting the pH of the ligand to 7.4.

It has been demonstrated that when all trajectory conformation frames are used, there is a significant improvement compared to docking studies using single (crystal) conformation or structures obtained from cluster analysis (Evangelista Falcon et al., 2019). Therefore, ensemble docking was performed using all frames from each MD run. To convert all frames from PDB to PDBQT the prepare_receptor.py script from the MGLTools package (https://ccsb.scripps.edu/mgltools/) was used.

A grid box was constructed to delimitate the search space. The binding pocket is the same as the binding of Mn^{2+} ion, so the grid box was defined as the smallest that encompassed this pocket in all protein frames. The best score (in kcal/mol) for each frame was recorded and analyzed in RStudio software.

2.14. Binding free energy

From the previous step, each replicate's best and worst complexes (lowest and highest Vina scores, respectively) were selected for MD analysis to evaluate complex stability in the solution. The MD protocol was the same as previously described for protein MD simulation. The MD simulation's ligand parameters were determined after inputting the ACPYPE server (https://www.bio2byte.be/acpype/) (Sousa da Silva and Vranken, 2012) using BCC as the charge method and GAFF2 as the atom type. The server provided all topology and parameter files required for MD simulations in the GROMACS software.

For each replicate, two MD simulations of protein-ligand were executed, totalising six MD simulations. The last 500 frames (50 ns) of the complexes were analysed using Molecular Mechanics/Generalized Born and Poisson-Boltzmann surface area (MM /GBSA and MM /PBSA, respectively) calculation, with all solvent molecules and Na^+ ions removed. The generalized Born method used was GB-Neck2 (igb=8) (Nguyen et al., 2013), and the internal dielectric constant was set to 4 (indi=4), which is the most accurate for highly charged binding pockets (as those containing ions) according to comparative studies (Hou et al., 2011).

In order to evaluate the residue's contribution in terms of energy (including the Mn^{2+} ion), the per-residue decomposition analyses of MM/PBSA were performed. The program used for these analyses was the new tool 'gmx_MMPBSA' (Valdés-Tresanco et al., 2021), which allows the user to directly use the output of GROMACS MD to calculate MM /GB (PB)SA. The 2D diagrams of protein-ligand interaction were generated using Discovery Studio Visualizer 2019 from Accelrys (https://discover.3ds.com/discovery-studio-visulizer-download).

3. Results

3.1. Assessment of host cell toxicity

We set the maximum concentration for toxicity assessment to 1000 μM for the acridones FAC21 and FAC22. Vero cell toxicity was analyzed 72 h post-treatment using an MTT cytotoxicity assay (Morgan, 1998). The compounds displayed cell viability above 50 % at the highest concentration of 500 μM. The FAC21 displayed a cytotoxicity concentration of 50 % (CC_{50}) of 1640 μM, and the FAC22 displayed CC_{50} = 1528 μM (Fig 2**A**).

3.2. Acridones promote an inhibitory activity against the oropouche virus

To evaluate whether OROV progeny reduction is affected by molecule concentration, we treated Vero cells with different concentrations of FAC21 or FAC22 and the viral progeny production was measured. We performed a cell and virus simultaneously treatment and infection assay during virus inoculation to examine the antiviral effect on virus entry steps, including virucidal (neutralizing) activity, and blockade of viral attachment and penetration to the cells. The viral progeny yields in non-treated cells reached 10^6 PFU/mL (Fig 2**B/C**). However, we found a significant decrease in dose-dependent viral titers in acridone-treated cells. To facilitate the visualization of viral inhibition, we added the percentage virus titer inhibition of the acridones represented under viral control to the right Y-axis. Anti-OROV potency in treated cells reached low-micromolar concentrations, with 50 % effective concentration
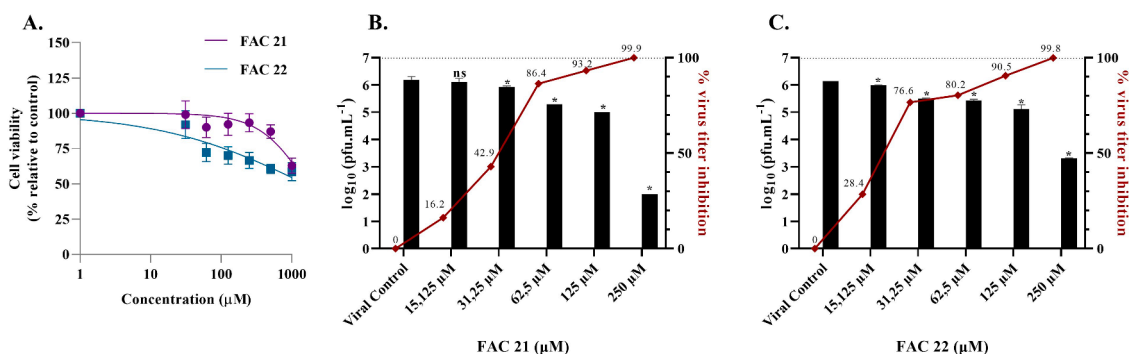
Fig. 2. Acridones have low cytotoxicity, and their effect on viral yield is concentration-dependent. (**A**) Cytotoxicity assay of the tested compounds in Vero cells. The cytotoxicity of acridones based on the dose-response was determined using MTT. The 50 % cytotoxic concentration (CC_{50}) was calculated for each compound using nonlinear regression analysis of GraphPad Prism software (version 8.0.1). (**B/C**) OROV production was measured in the presence of several dilutions of the tested compound in Vero cells, with an initial inoculum of MOI 0,1 under simultaneous treatment (bars chart and left axis). The diamond shape (◆) and the right axis represents percentages of viral inhibition under viral control. Error bars represent standard deviations. Values are the mean ± standard error obtained from three independent experiments.The dashed line indicates the detection limit for the viral titers assay. Asterisks indicate statistical significance between the control and each group as determined by two-way ANOVA and subsequent Dunnett's test (*, $p < 0.05$).

(EC_{50}) values of 33.03 ± 4.02 μM (Fig 2**B**) and 21.57 ± 3.83 μM (Fig 2**C**) for FAC21 and FAC22, respectively. Selectivity index (SI) was obtained from CC_{50}/EC_{50} ratio, with values of 49.65 and 70.83 for FAC21 and FAC22, respectively. The anti-OROV effect of acridones was apparent at 48 h post-infection (hpi).
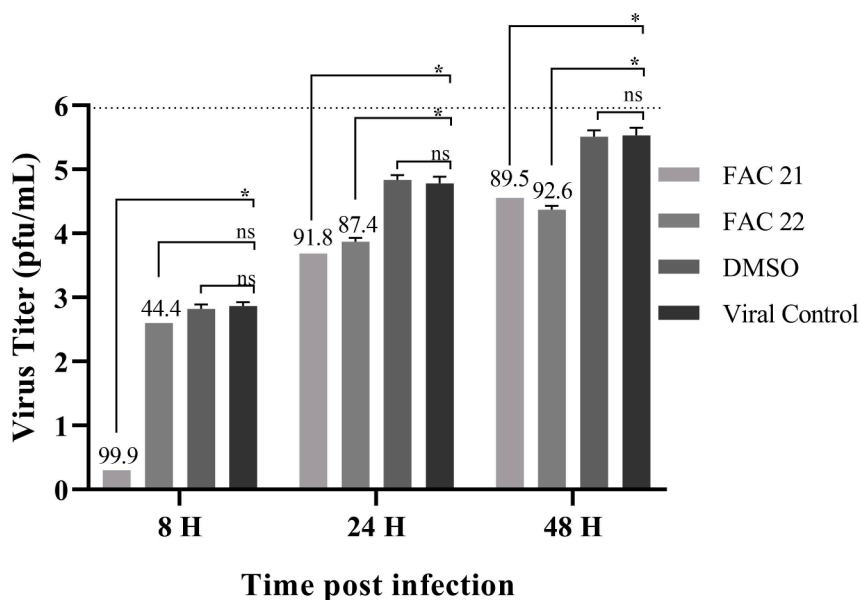
3.3. Acridones reduce Oropouche virus progeny yield

We next evaluated the effect of acridones on the production of infectious viral progeny in a growth kinetics inhibition assay (Fig 3), with ongoing treatment of 125 μM of acridones FAC21 or FAC22. A DMSO diluent control was also assessed to investigate possible interference with viral replication and rule out this possibility. A significant effect was observed for FAC21 at 8 and 24 hpi, being more pronounced in the first 8 h when the treatment with FAC21 decreased two logs compared to the viral control, equivalent to an inhibition of 99.9 %. Interestingly, FAC22 showed no significant inhibitory effect in the first 8 hpi.

However, the inhibitory effect was present at 24 and 48 hpi, with a one-log difference against the viral control. DMSO did not demonstrate significant activity compared to the viral control.

3.4. FAC21 and FAC22 as dsRNA intercalator

A dsRNA interaction assay was conducted to investigate the antiviral mode of action. The dsRNA is a replication intermediate of single-strand RNA viruses, and its structure and characteristics are similar in a range of single-stranded viruses families, therefore, is expected that if active, a compound that interacts with dsRNA from one virus, can interact with their similars (Koonin et al., 1993; Weber et al., 2006). In this context, employing the 3′ UTR region of JFH-1 HCV as a template, an amplicon flanked by a T7 promoter was produced and used for *in vitro* transcription, synthesizing a dsRNA molecule of 273 bp. 30 nM of dsRNA were incubated with FAC21 and FAC22 at 18.5 μM or with the controls (dimethyl sulfoxide 0.1 % as negative control and doxorubicin at 100 μM

Fig. 3. Antiviral activity of acridones in Oropouche Virus Progeny. Culture supernatants were harvested at the indicated time points. OROV production was measured in the presence of 125 μM dilution of the FAC21 or FAC22 in cells infected with MOI 0.1 by plaque forming assay. DMSO represents diluent control. Values are the mean ± standard error obtained from three independent experiments. The numbers above the bars indicate the percentage of virus inhibition (under the viral control). The dashed line indicates the detection limit for the viral titers assay. Asterisks indicate statistical significance between the control and each group as determined by two-way ANOVA and subsequent Dunnett's test (*, $p < 0.05$).

as positive control). After incubation, the samples were submitted to gel electrophoresis and as outcome, FAC21 and FAC22 demonstrated a modest interaction with the dsRNA, resulting in 84.5 % and 75.2 % of band intensity (up to 25 % of intercalation), respectively, when compared to the untreated control, quantified by densitometry (Fig 4). Notice that the band of the sample treated with doxorubicin (positive control of dsRNA interaction) does not appear in the gel.

3.5. Preparation of the OROV N-terminal endonuclease domain

The N-terminal endonuclease-His-tag fusion protein of OROV was expressed in *E. coli* Rosetta (DE3) cells and purified using a Ni-NTA affinity column. The pellet was resuspended in a lysis buffer containing 3 M Guanidine to access the His-Tag (**See Material and Methods**). After Ni-NTA purification, the respective protein fraction was dialysed against 10 mM Tris–HCl, 100 mM Sodium phosphate, pH 8. The 15 % SDS-PAGE gel (**S1 Fig**) indicates the purity of the protein.

3.6. Inhibitory effect of FAC21 and FAC22 against OROV N-terminal endonuclease domain

The N terminal region of the L segment sequence contains the endonuclease domain, which can bind and cleave RNA, and this activity is essential for transcription but not for replication steps in arenavirus (Amroun et al., 2017). In this sense, we investigated the inhibitory potential of the selected acridones (FAC21 and FAC22) against the OROV endonuclease activity. The activity assay was performed as described previously (Noble et al., 2012). As substrate for the OROV endonuclease, a labeled DNA (FAM-TCT CTA GCA GTG GCG CC-TAM) was used and the fluorescence intensities after cleavage were measured at 495 nm (excitation) and 520 nm (emission). Our results demonstrate that FAC21 efficiently inhibited the endonuclease activity by 95 % at a low tested concentration, and FAC22 showed no inhibitory potential (Fig 5A). FAC21 was further analysed regarding its potential to inhibit the catalytic activity of the target protein in a biochemical assay. FAC21 was tested using a concentration range of 0–90 μM (Fig 5B), and the molecule showed 100 % endonuclease inhibition at a final concentration of 70 μM presenting an IC50 value of 1.4 μM $\pm$ 0.3 (Fig 5C). Further experiments identified FAC21 as a competitive inhibitor of the OROV Endonuclease (Fig 5D), which means that FAC21 interact directly with amino acid residues located in the active site or the substrate binding region of the protein.
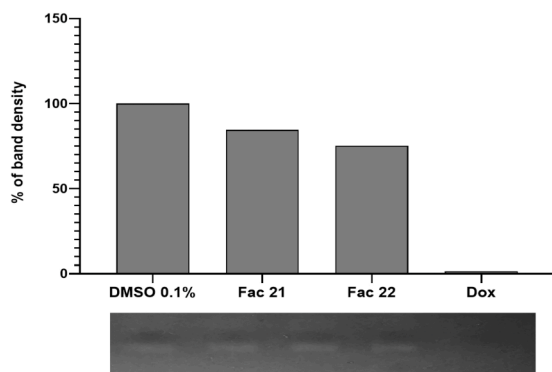
Fig. 4. Interaction of FAC21 and FAC22 with viral dsRNA. Thirty nanomoles of JFH-1 HCV dsRNA were incubated with FAC21 and 22 at 18.5 μM or the controls (DMSO 0.1 % and doxorubicin at 100 μM) for 45 min at room temperature. The reaction products were subjected to 1 % agarose 1X TAE electrophoresis gel containing Ethidium Bromide, followed by densitometry analysis on ImageJ.JS version 1.53j.

3.7. In silico studies of OROV endonuclease N-terminal domain-FAC21 interaction

In the absence of a three-dimensional model of the N-terminal region of the OROV endonuclease protein, the structure was modelled using I-TASSER server receiving a C-score of 1.62 (ranging from −5 to 2, with a higher value indicating a high confidence model), which was considered of quality by the MolProbity server. The clashscore (indicating the number of severe steric overlaps per 1000 atoms) gave a value of 3.03 (98th percentile, with the 100th percentile representing the best value among structures with comparable resolution) (**see S1 Table**). The Ramachandran plot (**S2 Fig**) showed eight phi/psi angular residuals as outliers, with 86.5 % and 95.5 % of all residuals in preferred and allowed regions, respectively. These results indicate that the protein modelled by I-TASSER has a high-quality conformation suitable for MD simulations. Subsequently, we carried out 3 sets of independent MD simulations (200 ns each). The model's flexibility during the MD simulation was monitored by calculating the RMSD and RMSF, which reveals the Cα RMSD below 1 Å (Fig 6A). The same can be observed for the RMSF, where the C-terminal region exhibited higher fluctuation (Fig 6B). The protein core (mainly the binding site, presented with a red circle in Fig 6C) is conserved among replicates MD trajectories. These results suggest that despite the expected differences among replicates, the ligand binding site structure is highly conserved when the protein is in solution (Fig 6C).

In previous work(Reguera et al., 2010), the authors described the N-terminal endonuclease as an elongated shape with a more exposed active site. The active site region is based in a region composed of anti-parallel beta-sheet and displays a remarkable similarity, although with no sequence homology; however, the amino acids responsible for the coordination of the Mn^{2+} ion are highly conserved (Reguera et al., 2010). Based on that, the same area was assumed for docking studies. Molecular docking and MD simulations of FAC21 with the OROV endonuclease N-terminal domain were performed in three sets of simulations (200 ns each).

The ensemble docking values per frame for the three replicates can be observed in **S3 Fig** and **S1 Text.** Replicate 1 presented the lowest (−6.9 kcal/mol) Vina binding score, while replicate 2 presented the highest (−3.9 kcal/mol). If we rank the lowest (highest) scores for each replicate, we get the following order: replicate 1 < replicate 2 < replicate 3 (replicate 1 < replicate 3 < replicate 2), see Table 1. These values of the Vina score agree with studies that have used Vina Docking as the previous step for MD of protein-ligand complexes (Anbarasu and Jayanthi, 2018; Malik et al., 2021; Sharma et al., 2022).

3.8. Binding free energy analysis

After the MD simulation of the best and worst Vina score complexes, RMSD and RMSF analyses of protein-FAC21 were performed (**S4, S5 Fig**). The last 50 ns (500 frames) were used for binding affinity energy calculation by MM/PB(GB)SA methods to evaluate if the ligand binding is energetically favoured and stable in solution. Table 2 shows the free energy of binding ($\Delta G_{binding}$) observed for MM/PB(GB)SA analysis of all six protein-ligand complexes. It can be observed that MM/PBSA provided better values than MM/GBSA analysis. However, in both calculation methods, the results were negative, suggesting that all complexes possess favourable $\Delta G_{binding}$ and are stable when in solution. **S6 Fig** shows the energy per frame of the MM/PBSA analysis.

The per-residue decomposition analysis of the complexes with the best Vina scores (Fig 7) shows that for replica 1 (Fig 7A), the residues contributing to the most attractive binding energy (less than −1 kcal/mol) are: Asp28, Asn31, His34, Asn35, Ser38, Arg39, Asn51 and Tyr49. For replica 2 (Fig 7B), using the same threshold, the residues are Asn31, His34, Asn35, Ser38, Arg39, Asp52 and Asn51, and for replica 3 (Fig 7C), we highlight residues Arg27, Leu30, Asn31, His34, Arg33, Asp77, Val93 and Leu129. The replicates commonly have Asn31 and His34,
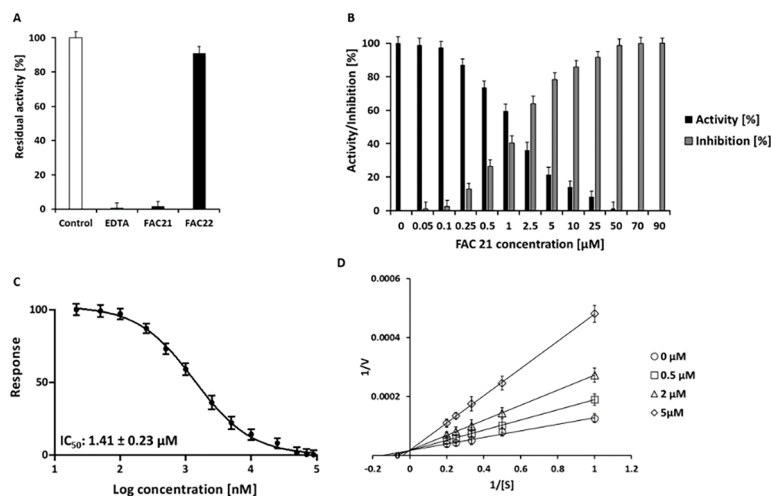
Fig. 5. Inhibition test, IC50 value determination and inhibition mode of the acridones FAC21 and FAC22 against OROV endonuclease. The enzyme activity was determined using the FAM-TCT CTA GCA GTG GCG CC-TAM DNA substrate, and the fluorescence intensities after cleavage were measured at 495 nm (excitation) and 520 nm (emission). (**A**) Primary inhibition test of FAC21 and FAC22 (50 μM) against the OROV endonuclease activity. EDTA (50 μM) was used as a known inhibitor control. (**B**) Normalized activity and inhibition of the endonuclease protein under the effect of FAC21. FAC21 was tested using a concentration range of 0–90 μM. (**C**) Dose–response curve for the IC50 value of FAC21 was determined by nonlinear regression. The normalized response [%] of OROV Endonuclease is plotted against the Log of the FAC21 concentration. The determined IC50 value is presented insert. (**D**) Inhibition mode of FAC21. The experiment was performed using different final concentrations of the inhibitor (0, 0.5, 2 and 5 μM) and titration of the substrate.The data were analyzed using a Lineweaver-Burk plot; therefore, the reciprocal of velocity (1/V) *vs* the reciprocal of the substrate concentration (1/[S]) was compared. Data shown are the mean ± standard deviation (SD) from three independent measurements ($n = 3$).
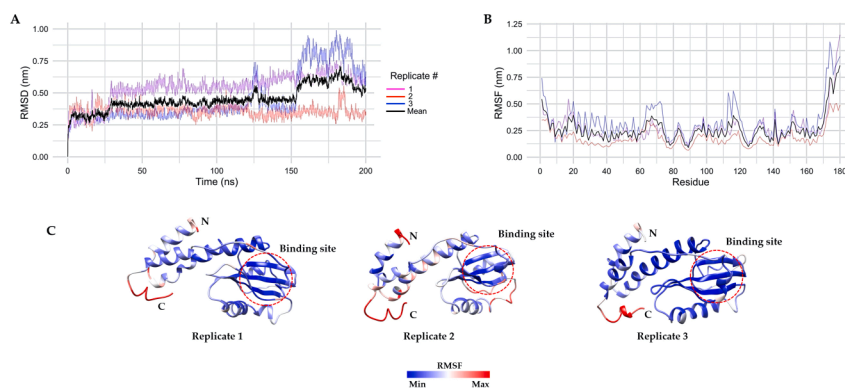
Fig. 6. MD simulations analysis of the N-terminal Endonuclease of OROV. (**A**) Cα RMSD evolution by 200 ns trajectory of three replicates (1 - purple, 2 - red, 3 - blue) and mean (black line). (**B**) RMSF analysis of three replicates using the same color scheme used in (A). It shows the average fluctuation per residue along the MD trajectory. (**C**) Ribbon representation of the three replicas coloured according to the RMSF values (with low and high fluctuation in blue and red, respectively). The Mn^{2+} binding site is shown in a red circle.

Table 1

Vina docking results in kcal/mol.

Replicate	Min	1st quartile	Median	Mean	3rd quartile	Max	Sd[†]
1	−6.9	−5.4	−5.3	−5.252	−5.1	−4.3	0.2922244
2	−6.6	−5.5	−5.2	−5.242	−5.0	−3.9	0.3255372
3	−6.5	−5.3	−5.1	−5.111	−4.9	−4.1	0.3256064

[†] Sd = standard deviation.

presenting a negative binding energy contribution. Likewise, in all replicates, the Mn^{+2} presented a positive value of the binding energy contribution. Among the three replicates, 48 common residues have binding free energy with negative values (**See S2 Table**).

The binding mode that presented the lowest $\Delta G_{binding}$ value is represented in Fig 7B. The representative frames of replicates 1, 2 and 3 are 1977 (−36.20 kcal/mol), 1884 (−43.63 kcal/mol) and 1868 (−42.34 kcal/mol), respectively. Most of the ligands were maintained near the Mn^{2+} ion (as shown in Fig 7), the protein active site. Also, the 2D

interaction analysis (Fig 7, right panel) shows that most interactions between the protein and the ligand are done through van der Waals, Alkyl or pi-alkyl and hydrogen bonds.

The analysis of MD simulation from complexes obtained from frames with the worst Vina score values can be seen in **S2 Text** and **S7 Fig**.

4. Discussion

The high virulence of viruses and the absence of effective therapies

Table 2

MM/PB(GB)SA results.

Replicate	MM/PBSA[‡]		MM/GBSA[‡]	
	Complex with Best Vina Scores[†]	Complex with Worst Vina Scores[†]	Complex with Best Vina Scores[†]	Complex with Worst Vina Scores[†]
1	−30.73 ± 2.52	−14.21 ± 5.21	−21.96 ± 3.12	−9.29 ± 4.34
2	−34.17 ± 3.19	−23.44 ± 2.89	−32.04 ± 4.18	−18.91 ± 4.31
3	−35.82 ± 2.42	−22.09 ± 3.84	−24.48 ± 2.74	−14.37 ± 3.22

[‡] Average ± standard deviation.

[†] The best score is the lower Vina score, and the worst is the higher one.

pose an ongoing threat to public health. Oropouche fever is an endemic zoonotic infection in South and Central American regions, characterized by an intense and self-limiting febrile condition. Despite infecting numerous individuals (more than half a million) (Sakkas et al., 2018), it has long been a neglected disease. Although OROV represents a public health concern in some countries, this virus is still poorly studied and underreported since its symptomatology can be easily confused with other febrile illnesses(Pereira et al., 2021). No antiviral drugs are available to treat OROV infections. Hence, there is an urgent need for proper antiviral therapies to control possible forthcoming outbreaks.

The antiviral impact of acridones has been depicted, and the action range of this class of alkaloids changes depending on the type of viral genome (double-stranded DNA genome or RNA infections) (Sepulveda et al., 2013). Natural and synthetic acridone-based substances have been

recognized as multi-targeted agents with a broad spectrum of biomedical potential (Belmont et al., 2007; Sepulveda et al., 2013). Several natural acridones from *Rutaceae* plants have shown notable antiviral action against DNA viruses from the *Herpesviridae* family (Chansriniyom et al., 2009; Itoigawa et al., 2003; Takemura et al., 1995; Yamamoto et al., 1989). Acridones have demonstrated action against RNA viruses from different families, primarily described as representatives of the *Flaviviridae* family (Campos et al., 2017; Fujiwara et al., 1999; Loddo et al., 2018; Mazzucco et al., 2015; Sepúlveda et al., 2008; Stankiewicz-Drogoń et al., 2010; Stankiewicz-Drogon et al., 2008; Turpin et al., 1998).

Based on the antiviral history of this class of alkaloids, we investigated the anti-OROV potential of FAC21 and FAC22. Our results showed that FAC21 strongly inhibited the virus during the first 8 hpi, with an inhibition greater than two logs. According to our findings, FAC21 demonstrated the ability to partially intercalate into dsRNA; however, surprisingly, it inhibited up to 95 % of the endonuclease protein activity, as observed in the OROV endonuclease activity assay. On the other hand, despite the molecular similarity between FAC21 and FAC22, different results were observed with FAC22. Our results indicated that FAC22 progressively inhibited viral activity, reaching an inhibition greater than one log at 48 hpi. According to our findings, FAC22 demonstrated a more pronounced ability to partially intercalate into dsRNA. However, it did not inhibit the endonuclease activity of OROV. The results of MD simulations, docking, and binding free energy analysis suggested the interaction of FAC21 with the OROV Endonuclease in the binding site. Thus, if FAC21 interacts in this protein region with high affinity and stability, it is expected to limit RNA access and binding, promoting endonuclease inhibition.
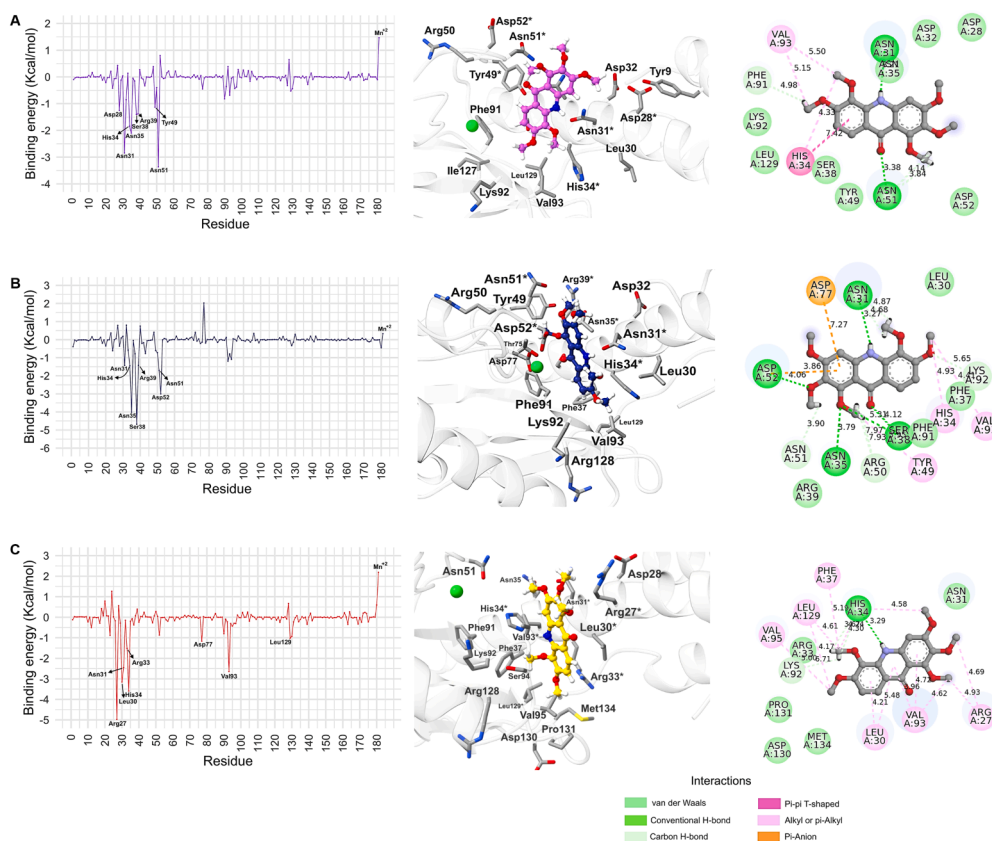
Fig. 7. MD of complexes that presented the best Vina score values. The figure is organised by row: Per-residue decomposition analysis from MM/PBSA calculation; the best $\Delta G_{binding}$ binding mode and 2D interactions between ligand and protein residues. Ligand binding mode that presents the lower $\Delta G_{binding}$ residues less than 5 Å away from the FAC21(in gray stick): (**A**) replica 1, (**B**) replica 2, and (**C**) replica 3. Residues are numbered according to the protein sequence, and Mn^{2+} is 181. The residues marked with * in the middle panel appeared with $\Delta G_{binding}$ lower than −1 kcal/mol in per-residue MM/PBSA analysis. The Mn^{2+} is represented by a green ball in the middle panel figures.

Several studies have reported that acridones may play an inhibitory role in viral replication. Some studies even highlight the potential of acridones to intercalate into dsRNA (Campos et al., 2017; Silakari, 2018), serving as inspiration for investigating this potential of the acridones FAC21 and FAC22 in dsRNA intercalation. However, other studies have focused on identifying the inhibition of enzyme activities related to viral replication, such as helicases or polymerases (Campos et al., 2017; Manfroni et al., 2009; Stankiewicz-Drogoń et al., 2010). Due to these previous findings, we directed our studies to identify actions in similar mechanisms, such as the potential of FAC21 and FAC22 in dsRNA intercalation and the inhibition of OROV endonuclease. While both acridones showed potential for intercalation, only FAC21 exhibited an inhibitory potential on OROV endonuclease. However, other modes of action are likely involved, such as targeting cellular components, since acridone derivatives, such as cycloferon (CMA), are described as compounds that can induce the interferon pathway (Kovalenko et al., 2000; Taylor et al., 1980); however, further investigation is needed.

The results observed in viral release assays (Figs 2 and 3) reinforce the antiviral activity of FAC21 and FAC22. The acridones exhibited near or up to 90 % inhibition in OROV release (pfu level) at different concentrations. This assay was performed 8–48 h after treatment. The inhibition of replication was observed early, at 8 h after treatment for FAC21 and later (24hpi) for FAC22. These results could indicate that, after 24 h, FACs have significantly influenced OROV replication, and there might be some interaction between the acridone and the viral RNA preventing the release of new viral particles.

In conclusion, in the present study, we demonstrated that the acridones FAC21 and FAC22 selectively inhibit the *in vitro* infection of OROV, interfering specifically with intracellular virus replication. The endonuclease of OROV appears to be partially involved in the anti-OROV activity of acridone. However, other unidentified targets affecting viral RNA synthesis must also be active to achieve the virus yield inhibition produced by the inhibitor, suggesting a dual mechanism of antiviral action, which may, to some extent, be caused by ds-RNA intercalation. Acridones are broad-spectrum antiviral agents promising for managing viruses lacking specific chemotherapy. The inhibitory effect of acridones against OROV merits further testing of these compounds with other medically relevant RNA viruses.

Funding sources

CRediT authorship contribution statement

Marielena Vogel Saivish: Methodology, Validation, Investigation, Formal analysis, Writing – original draft, Writing – review & editing, Visualization. **Gabriela de Lima Menezes:** Methodology, Validation, Investigation, Formal analysis, Writing – original draft, Writing – review & editing, Visualization. **Roosevelt Alves da Silva:** Supervision, Writing – review & editing, Resources. **Leticia Ribeiro de Assis:** Funding acquisition. **Igor da Silva Teixeira:** Investigation. **Umberto Laino Fulco:** Supervision, Writing – review & editing, Resources. **Clarita Maria Secco Avilla:** Investigation. **Raphael Josef Eberle:** Investigation. **Igor de Andrade Santos:** Investigation. **Karolina Korostov:** Investigation. **Mayara Lucia Webber:** Investigation. **Gislaine Celestino Dutra da Silva:** Investigation. **Maurício Lacerda Nogueira:** Supervision, Writing – review & editing, Resources, Funding acquisition. **Ana Carolina Gomes Jardim:** Investigation. **Luis Octavio Regasin:** Supervision, Writing – review & editing. **Mônika Aparecida Coronado:** Writing – original draft, Supervision, Writing – review & editing. **Carolina Colombelli Pacca:** Writing – original draft, Supervision, Writing – review & editing, Funding acquisition.

Declaration of Competing Interest

The authors declare the following financial interests/personal relationships which may be considered as potential competing interests: Mauricio Lacerda Nogueira reports financial support was provided by The Coordinating Research on Emerging Arboviral Threats Encompassing the Neotropics.

Data availability

Data will be made available on request.

Acknowledgement

Supplementary materials

Supplementary material associated with this article can be found, in the online version, at doi:10.1016/j.crmicr.2023.100217.

References

Abraham, M.J., Murtola, T., Schulz, R., Páll, S., Smith, J.C., Hess, B., Lindahl, E., 2015. GROMACS: high performance molecular simulations through multi-level parallelism from laptops to supercomputers. SoftwareX 1–2, 19–25. https://doi.org/10.1016/j.softx.2015.06.001.

Almeida, G.M., Souza, J.P., Mendes, N.D., Pontelli, M.C., Pinheiro, N.R., Nogueira, G.O., Cardoso, R.S., Paiva, I.M., Ferrari, G.D., Veras, F.P., Cunha, F.Q., Horta-Junior, J.A.C., Alberici, L.C., Cunha, T.M., Podolsky-Gondim, G.G., Neder, L., Arruda, E., Sebollela, A., 2021. Neural infection by oropouche virus in adult human brain slices induces an inflammatory and toxic response. Front. Neurosci. 15.

Amroun, A., Priet, S., de Lamballerie, X., Quérat, G., 2017. Bunyaviridae RdRps: structure, motifs, and RNA synthesis machinery. Crit. Rev. Microbiol. 43, 753–778. https://doi.org/10.1080/1040841X.2017.1307805.

Anbarasu, K., Jayanthi, S., 2018. Identification of curcumin derivatives as human LMTK3 inhibitors for breast cancer: a docking, dynamics, and MM/PBSA approach. 3 Biotech 8, 228. https://doi.org/10.1007/s13205-018-1239-6.

Azevedo, R.S., da, S., Nunes, M.R.T., Chiang, J.O., Bensabath, G., Vasconcelos, H.B., Pinto, A.Y., das, N., Martins, L.C., Monteiro, H.A., de, O., Rodrigues, S.G., Vasconcelos, P.F., da, C., 2007. Reemergence of Oropouche fever, northern Brazil. Emerg. Infect. Dis. 13, 912–915. https://doi.org/10.3201/eid1306.061114.

Bastos, M., de, S., Figueiredo, L.T.M., Naveca, F.G., Monte, R.L., Lessa, N., Pinto de Figueiredo, R.M., Gimaque, J.B., de, L., Pivoto João, G., Ramasawmy, R., Mourão, M.P.G., 2012. Identification of Oropouche Orthobunyavirus in the cerebrospinal fluid of three patients in the Amazonas, Brazil. Am. J. Trop. Med. Hyg. 86, 732–735. https://doi.org/10.4269/ajtmh.2012.11-0485.

Bastos, M.S., Lessa, N., Naveca, F.G., Monte, R.L., Braga, W.S., Figueiredo, L.T.M., Ramasawmy, R., Mourão, M.P.G., 2014. Detection of Herpesvirus, Enterovirus, and Arbovirus infection in patients with suspected central nervous system viral infection in the Western Brazilian Amazon. J. Med. Virol. 86, 1522–1527. https://doi.org/10.1002/jmv.23953.

Belmont, P., Bosson, J., Godet, T., Tiano, M., 2007. Acridine and Acridone derivatives, anticancer properties and synthetic methods: where are we now? Anticancer Agents Med. Chem. 7, 139–169.

Berendsen, H.J.C., Postma, J.P.M., van Gunsteren, W.F., DiNola, A., Haak, J.R., 1984. Molecular dynamics with coupling to an external bath. J. Chem. Phys. 81, 3684–3690. https://doi.org/10.1063/1.448118.

Campos, G.R.F., Bittar, C., Jardim, A.C.G., Shimizu, J.F., Batista, M.N., Paganini, E.R., Assis, L.R.de, Bartlett, C., Harris, M., Bolzani, V.da S., Regasini, L.O., Rahal, P., 2017. Hepatitis C virus *in vitro* replication is efficiently inhibited by acridone Fac4. J. Gen. Virol. 98, 1693–1701. https://doi.org/10.1099/jgv.0.000808.

Cardoso, B.F., Serra, O.P., Heinen, L.B.da S., Zuchi, N., Souza, V.C.de, Naveca, F.G., Santos, M.A.M.dos, Slhessarenko, R.D., 2015. Detection of Oropouche virus segment S in patients and inCulex quinquefasciatus in the state of Mato Grosso, Brazil. Mem. Inst. Oswaldo Cruz 110, 745–754. https://doi.org/10.1590/0074-02760150123.

Chansriniyom, C., Ruangrungsi, N., Lipipun, V., Kumamoto, T., Ishikawa, T., 2009. Isolation of acridone alkaloids and N-[(4-*monoterpenyloxy*)*phenylethyl*]-substituted sulfur-containing propanamide derivatives from Glycosmis parva and their anti-herpes simplex virus activity. Chem. Pharm. Bull. (Tokyo) 57, 1246–1250. https://doi.org/10.1248/cpb.57.1246.

da Costa, V.G., de Rezende Féres, V.C., Saivish, M.V., de Lima Gimaque, J.B., Moreli, M. L., 2017. Silent emergence of Mayaro and Oropouche viruses in humans in Central Brazil. Int. J. Infect. Dis. IJID Off. Publ. Int. Soc. Infect. Dis. 62, 84–85. https://doi.org/10.1016/j.ijid.2017.07.016.

de Souza Luna, L.K., Rodrigues, A.H., Santos, R.I.M., Sesti-Costa, R., Criado, M.F., Martins, R.B., Silva, M.L., Delcaro, L.S., Proença-Modena, J.L., Figueiredo, L.T.M., Acrani, G.O., Arruda, E., 2017. Oropouche virus is detected in peripheral blood leukocytes from patients. J. Med. Virol. 89, 1108–1111. https://doi.org/10.1002/jmv.24722.

Evangelista Falcon, W., Ellingson, S.R., Smith, J.C., Baudry, J., 2019. Ensemble docking in drug discovery: how many protein configurations from molecular dynamics simulations are needed to reproduce known ligand binding? J. Phys. Chem. B 123, 5189–5195. https://doi.org/10.1021/acs.jpcb.8b11491.

Fujiwara, M., Okamoto, Mika, Okamoto, Masayuki, Watanabe, M., Machida, H., Shigeta, S., Konno, K., Yokota, T., Baba, M., 1999. Acridone derivatives are selective inhibitors of HIV-1 replication in chronically infected cells. Antiviral Res. 43, 189–199. https://doi.org/10.1016/S0166-3542(99)00045-5.

Gensicka-Kowalewska, M., Cholewiński, G., Dzierzbicka, K., 2017. Recent developments in the synthesis and biological activity of acridine/acridone analogues. RSC Adv. 7, 15776–15804. https://doi.org/10.1039/C7RA01026E.

Gláz, E.T., Szolgay, E., Stöger, I., Tálas, M., 1973. Antiviral activity and induction of interferon-like substance by Quinacrine and Acranil. Antimicrob. Agents Chemother. 3, 537–541.

Gutierrez, B., Wise, E.L., Pullan, S.T., Logue, C.H., Bowden, T.A., Escalera-Zamudio, M., Trueba, G., Nunes, M.R.T., Faria, N.R., Pybus, O.G., 2020. Evolutionary dynamics of Oropouche virus in South America. J. Virol. 94, e01119–e01127. https://doi.org/10.1128/JVI.01127-19.

Herath, H.M.T.B., Müller, K., Diyabalanage, H.V.K., 2004. Synthesis of acrimarins from 1,3,5-trioxygenated-9-acridone derivatives. J. Heterocycl. Chem. 41, 23–28. https://doi.org/10.1002/jhet.5570410104.

Hess, B., Bekker, H., Berendsen, H.J.C., Fraaije, J.G.E.M., 1997. LINCS: a linear constraint solver for molecular simulations. J. Comput. Chem. 18, 1463–1472. https://doi.org/10.1002/(SICI)1096-987X(199709)18:12<1463::AID−JCC4>3.0.CO;2-H.

Hockney, R.W., Goel, S.P., Eastwood, J.W., 1974. Quiet high-resolution computer models of a plasma. J. Comput. Phys. 14, 148–158. https://doi.org/10.1016/0021-9991(74)90010-2.

Hou, T., Wang, J., Li, Y., Wang, W., 2011. Assessing the performance of the MM/PBSA and MM/GBSA methods. 1. the accuracy of binding free energy calculations based on molecular dynamics simulations. J. Chem. Inf. Model. 51, 69–82. https://doi.org/10.1021/ci100275a.

Hutter, J., 2012. Car-Parrinello molecular dynamics: car-Parrinello molecular dynamics. Wiley Interdiscip. Rev. Comput. Mol. Sci. 2, 604–612. https://doi.org/10.1002/wcms.90.

Itoigawa, M., Ito, C., Wu, T.S., Enjo, F., Tokuda, H., Nishino, H., Furukawa, H., 2003. Cancer chemopreventive activity of acridone alkaloids on Epstein–Barr virus activation and two-stage mouse skin carcinogenesis. Cancer Lett. 193, 133–138. https://doi.org/10.1016/S0304-3835(03)00008-9.

Koonin, E.V., Dolja, V.V., Morris, T.J., 1993. Evolution and taxonomy of positive-strand RNA viruses: implications of comparative analysis of amino acid sequences. Crit. Rev. Biochem. Mol. Biol. 28, 375–430. https://doi.org/10.3109/10409239309078440.

Kovalenko, A.L., Kazakov, V.I., Slita, A.V., Zarubaev, V.V., Sukhinin, V.P., 2000. [Intracellular localization of cycloferon, its binding with DNA and stimulation of cytokines expression after exposure to cycloferon]. Tsitologiia 42, 659–664.

Krawczyk, M., Wasowska-Lukawska, M., Oszczapowicz, I., Boguszewska-Chachulska, A. M., 2009. Amidinoanthracyclines – a new group of potential anti-hepatitis C virus compounds. Biol. Chem. 390 https://doi.org/10.1515/BC.2009.040.

Loddo, R., Francesconi, V., Laurini, E., Boccardo, S., Aulic, S., Fermeglia, M., Pricl, S., Tonelli, M., 2018. 9-Aminoacridine-based agents impair the bovine viral diarrhea virus (BVDV) replication targeting the RNA-dependent RNA polymerase (RdRp). Bioorg. Med. Chem. 26, 855–868. https://doi.org/10.1016/j.bmc.2018.01.001.

Malik, A., Naz, A., Ahmad, S., Hafeez, M., Awan, F.M., Jafar, T.H., Zahid, A., Ikram, A., Rauff, B., Hassan, M., 2021. Inhibitory potential of phytochemicals on interleukin-6-mediated T-Cell reduction in COVID-19 patients: a computational approach. Bioinforma. Biol. Insights 15. https://doi.org/10.1177/11779322211021430, 11779322211021430.

Manfroni, G., Paeshuyse, J., Massari, S., Zanoli, S., Gatto, B., Maga, G., Tabarrini, O., Cecchetti, V., Fravolini, A., Neyts, J., 2009. Inhibition of subgenomic hepatitis C

virus RNA replication by acridone derivatives: identification of an NS3 helicase inhibitor. J. Med. Chem. 52, 3354–3365. https://doi.org/10.1021/jm801608u.

Mazzucco, M.B., Talarico, L.B., Vatansever, S., Carro, A.C., Fascio, M.L., D'Accorso, N.B., García, C.C., Damonte, E.B., 2015. Antiviral activity of an N-allyl acridone against dengue virus. J. Biomed. Sci. 22, 29. https://doi.org/10.1186/s12929-015-0134-2.

Morgan, D.M., 1998. Tetrazolium (MTT) assay for cellular viability and activity. Methods Mol. Biol. Clifton NJ 79, 179–183. https://doi.org/10.1385/0-89603-448-8:179.

Motulsky, H., Christopoulos, A., n.d. Fitting models to biological data using linear and nonlinear regression 351.

Mourão, M.P.G., Bastos, M.S., Gimaque, J.B.L., Mota, B.R., Souza, G.S., Grimmer, G.H.N., Galusso, E.S., Arruda, E., Figueiredo, L.T.M., 2009. Oropouche fever outbreak, Manaus, Brazil, 2007–2008. Emerg. Infect. Dis. 15, 2063–2064. https://doi.org/10.3201/eid1512.090917.

Nguyen, H., Roe, D.R., Simmerling, C., 2013. Improved generalized born solvent model parameters for protein simulations. J. Chem. Theory Comput. 9, 2020–2034. https://doi.org/10.1021/ct3010485.

Noble, E., Cox, A., Deval, J., Kim, B., 2012. Endonuclease substrate selectivity characterized with full-length PA of influenza A virus polymerase. Virology 433, 27–34. https://doi.org/10.1016/j.virol.2012.07.008.

O'Boyle, N.M., Banck, M., James, C.A., Morley, C., Vandermeersch, T., Hutchison, G.R., 2011. Open Babel: an open chemical toolbox. J. Cheminformatics 3, 33. https://doi.org/10.1186/1758-2946-3-33.

Olsson, M.H.M., Søndergaard, C.R., Rostkowski, M., Jensen, J.H., 2011. PROPKA3: consistent treatment of internal and surface residues in Empirical p K_a predictions. J. Chem. Theory Comput. 7, 525–537. https://doi.org/10.1021/ct100578z.

Pereira, T.N., Virginio, F., Souza, J.I., Moreira, L.A., 2021. Emergent Arboviruses: a review about Mayaro virus and Oropouche orthobunyavirus. Front. Trop. Dis. 2.

Pettersen, E.F., Goddard, T.D., Huang, C.C., Couch, G.S., Greenblatt, D.M., Meng, E.C., Ferrin, T.E., 2004. UCSF Chimera - a visualization system for exploratory research and analysis. J. Comput. Chem. 25, 1605–1612. https://doi.org/10.1002/jcc.20084.

Pettersen, E.F., Goddard, T.D., Huang, C.C., Meng, E.C., Couch, G.S., Croll, T.I., Morris, J. H., Ferrin, T.E., 2021. UCSF ChimeraX : structure visualization for researchers, educators, and developers. Protein Sci. 30, 70–82. https://doi.org/10.1002/pro.3943.

Pinheiro, F.P., Rocha, A.G., Freitas, R.B., Ohana, B.A., Travassos da Rosa, A.P., Rogério, J.S., Linhares, A.C., 1982a. [Meningitis associated with Oropouche virus infections]. Rev. Inst. Med. Trop. Sao Paulo 24, 246–251.

Pinheiro, F.P., Travassos da Rosa, A.P., Travassos da Rosa, J.F., Ishak, R., Freitas, R.B., Gomes, M.L., LeDuc, J.W., Oliva, O.F., 1981. Oropouche virus. I. A review of clinical, epidemiological, and ecological findings. Am. J. Trop. Med. Hyg. 30, 149–160.

Pinheiro, Francisco de Paula, Rocha, Arnaldo G, Freitas, Ronaldo Barros de, Ohana, Benjamin A, Rosa, Amélia Paes de Andrade Travassos da, Rogério, Juvenal S, Linhares, Alexandre da Costa, 1982b. Meningite associada ás infecções por vírus Oropouche. Meningite Assoc. Ás Infecções Por Vírus Oropouche 4, 246–251.

Reguera, J., Weber, F., Cusack, S., 2010. Bunyaviridae RNA polymerases (L-protein) have an N-terminal, influenza-like endonuclease domain, essential for viral cap-dependent transcription. PLoS Pathog. 6, e1001101 https://doi.org/10.1371/journal.ppat.1001101.

Romero-Alvarez, D., Escobar, L.E., 2018. Oropouche fever, an emergent disease from the Americas. Microbes Infect. 20, 135–146. https://doi.org/10.1016/j.micinf.2017.11.013.

RStudio Team, 2021. RStudio: Integrated Development Environment for R. RStudio, PBC, Boston, MA.

Sakkas, H., Bozidis, P., Franks, A., Papadopoulou, C., 2018. Oropouche fever: a review. Viruses 10, 175. https://doi.org/10.3390/v10040175.

Sánchez, I., Reches, R., Caignard, D.H., Renard, P., Pujol, M.D., 2006. Synthesis and biological evaluation of modified acridines: the effect of N- and O- substituent in the nitrogenated ring on antitumor activity. Eur. J. Med. Chem. 41, 340–352. https://doi.org/10.1016/j.ejmech.2005.11.006.

Santos, R.I., Bueno-Júnior, L.S., Ruggiero, R.N., Almeida, M.F., Silva, M.L., Paula, F.E., Correa, V.M.A., Arruda, E., 2014. Spread of Oropouche virus into the central nervous system in mouse. Viruses 6, 3827–3836. https://doi.org/10.3390/v6103827.

Sepulveda, C.S., Fascio, M.L., Garcia, C.C., D'Accorso, N.B., Damonte, E.B., 2013. Acridones as antiviral agents: synthesis, chemical and biological properties. Curr. Med. Chem. 20, 2402–2414.

Sepúlveda, C.S., Fascio, M.L., Mazzucco, M.B., Palacios, M.L.D., Pellón, R.F., García, C.C., D'Accorso, N.B., Damonte, E.B., 2008. Synthesis and evaluation of N-substituted acridones as antiviral agents against Haemorrhagic fever viruses. Antivir. Chem. Chemother. 19, 41–47. https://doi.org/10.1177/095632020801900106.

Sharma, A., Vora, J., Patel, D., Sinha, S., Jha, P.C., Shrivastava, N., 2022. Identification of natural inhibitors against prime targets of SARS-CoV-2 using molecular docking, molecular dynamics simulation and MM-PBSA approaches. J. Biomol. Struct. Dyn. 40, 3296–3311. https://doi.org/10.1080/07391102.2020.1846624.

Silakari, O., 2018. Key Heterocycle Cores For Designing Multitargeting Molecules. Elsevier.

Silva, S., Shimizu, J.F., Oliveira, D.M.de, Assis, L.R.de, Bittar, C., Mottin, M., Sousa, B.K. de P., Mesquita, N.C.de M.R., Regasini, L.O., Rahal, P., Oliva, G., Perryman, A.L., Ekins, S., Andrade, C.H., Goulart, L.R., Sabino-Silva, R., Merits, A., Harris, M., Jardim, A.C.G., 2019. A diarylamine derived from anthranilic acid inhibits ZIKV replication. Sci. Rep. 9, 17703. https://doi.org/10.1038/s41598-019-54169-z.

Silva-Caso, W., Aguilar-Luis, M.A., Palomares-Reyes, C., Mazulis, F., Weilg, C., del Valle, L.J., Espejo-Evaristo, J., Soto-Febres, F., Martins-Luna, J., del Valle-Mendoza, J., 2019. First outbreak of Oropouche fever reported in a non-endemic western region of the Peruvian Amazon: molecular diagnosis and clinical characteristics. Int. J. Infect. Dis. 83, 139–144. https://doi.org/10.1016/j.ijid.2019.04.011.

Sousa da Silva, A.W., Vranken, W.F., 2012. ACPYPE - antechamber python parser interface. BMC Res. Notes 5, 367. https://doi.org/10.1186/1756-0500-5-367.

Stankiewicz-Drogoń, A., Dörner, B., Erker, T., Boguszewska-Chachulska, A.M., 2010. Synthesis of new acridone derivatives, inhibitors of NS3 helicase, which efficiently and specifically inhibit subgenomic HCV replication. J. Med. Chem. 53, 3117–3126. https://doi.org/10.1021/jm901741p.

Stankiewicz-Drogon, A., Palchykovska, L.G., Kostina, V.G., Alexeeva, I.V., Shved, A.D., Boguszewska-Chachulska, A.M., 2008. New acridone-4-carboxylic acid derivatives as potential inhibitors of Hepatitis C virus infection. Bioorg. Med. Chem. 16, 8846–8852. https://doi.org/10.1016/j.bmc.2008.08.074.

Takemura, Y., Ju-ichi, M., Ito, C., Furukawa, H., Tokuda, H., 1995. Studies on the inhibitory effects of some acridone alkaloids on Epstein-Barr Virus activation. Planta Med. 61, 366–368. https://doi.org/10.1055/s-2006-958104.

Taylor, J.L., Schoenherr, C., Grossberg, S.E., 1980. High-yield interferon induction by 10-carboxymethyl-9-acridanone in mice and hamsters. Antimicrob. Agents Chemother. https://doi.org/10.1128/aac.18.1.20.

Tonelli, M., Vettoretti, G., Tasso, B., Novelli, F., Boido, V., Sparatore, F., Busonera, B., Ouhtit, A., Farci, P., Blois, S., Giliberti, G., La Colla, P., 2011. Acridine derivatives as anti-BVDV agents. Antiviral Res. 91, 133–141. https://doi.org/10.1016/j.antiviral.2011.05.005.

Travassos da Rosa, J.F., de Souza, W.M., Pinheiro, F., de, P., Figueiredo, M.L., Cardoso, J. F., Acrani, G.O., Nunes, M.R.T., 2017. Oropouche Virus: clinical, epidemiological, and molecular aspects of a neglected orthobunyavirus. Am. J. Trop. Med. Hyg. 96, 1019–1030. https://doi.org/10.4269/ajtmh.16-0672.

Trott, O., Olson, A.J., 2010. AutoDock Vina: improving the speed and accuracy of docking with a new scoring function, efficient optimization, and multithreading. J. Comput. Chem. 31, 455–461. https://doi.org/10.1002/jcc.21334.

Turpin, J.A., Buckheit, R.W., Derse, D., Hollingshead, M., Williamson, K., Palamone, C., Osterling, M.C., Hill, S.A., Graham, L., Schaeffer, C.A., Bu, M., Huang, M., Cholody, W.M., Michejda, C.J., Rice, W.G., 1998. Inhibition of acute-, latent-, and chronic-phase human immunodeficiency virus type 1 (HIV-1) replication by a bistriazoloacridone analog that selectively inhibits HIV-1 transcription. Antimicrob. Agents Chemother. 42, 487–494.

Valdés-Tresanco, M.S., Valdés-Tresanco, M.E., Valiente, P.A., Moreno, E., 2021. gmx_MMPBSA: a new tool to perform end-state free energy calculations with GROMACS. J. Chem. Theory Comput. 17, 6281–6291. https://doi.org/10.1021/acs.jctc.1c00645.

Weber, F., Wagner, V., Rasmussen, S.B., Hartmann, R., Paludan, S.R., 2006. Double-stranded RNA is produced by positive-strand RNA viruses and DNA viruses but not in detectable amounts by negative-strand RNA viruses. J. Virol. 80, 5059–5064. https://doi.org/10.1128/jvi.80.10.5059-5064.2006.

Williams, C.J., Headd, J.J., Moriarty, N.W., Prisant, M.G., Videau, L.L., Deis, L.N., Verma, V., Keedy, D.A., Hintze, B.J., Chen, V.B., Jain, S., Lewis, S.M., Arendall, W.B., Snoeyink, J., Adams, P.D., Lovell, S.C., Richardson, J.S., Richardson, D.C., 2018. MolProbity: more and better reference data for improved all-atom structure validation: PROTEIN SCIENCE.ORG. . Protein Sci. 27, 293–315. https://doi.org/10.1002/pro.3330.

Yamamoto, N., Furukawa, H., Ito, Y., Yoshida, S., Maeno, K., Nishiyama, Y., 1989. Anti-herpesvirus activity of citrusinine-I, a new acridone alkaloid, and related compounds. Antiviral Res. 12, 21–36. https://doi.org/10.1016/0166-3542(89)90065-X.